Second-harmonic and reflectance-anisotropy spectroscopy of vicinal Si(001)/SiO_2 interfaces: Experiment and simplified microscopic model

Jinhee Kwon and M. C. Downer
Texas Materials Institute, University of Texas at Austin, Austin, Texas 78712-1081, USA
and Department of Physics, University of Texas at Austin, Austin, Texas 78712-1081, USA

B. S. Mendoza
Centro de Investigaciones en Optica, León, Guanajuato, Mexico

(Received 28 January 2006; revised manuscript received 17 April 2006; published 30 May 2006)

We directly compare experimental second-harmonic generation (SHG) spectra and reflectance-anisotropy spectra (RAS) of native-oxidized vicinal Si(001) interfaces with off-cut angles $\zeta=0°$, 4°, 6°, 8°, and 10° from (001) toward [110]. We fit the measured azimuthal rotational-dependence of *p*-in/*p*-out SHG at two-photon energies 2.8 eV$<\hbar\omega<$3.5 eV including the E_1 critical point resonance using a simplified bond hyperpolarizability model. The model includes dipolar contributions from tetrahedrally coordinated interfacial bonds as well as quadrupolar contributions from the Si bulk. The fit yields complex axial hyperpolarizability spectra $\beta_{\|,\|,\|}(2\omega)$ and averaged bond angles of the interfacial back-edge, terrace-edge and step-edge bonds, and bulk quadrupolar hyperpolarizability $\delta_{\|,\|,\|}(2\omega)$. The fitted microscopic model accurately reproduces measured *s*-in/*p*-out SHG spectra. We then used a Miller's rule approximation to generate axial linear polarizability spectra $\alpha_{\|}(\omega)$ from the fitted $\beta_{\|,\|,\|}(2\omega)$. The measured RAS was satisfactorily reproduced within the same photon energy range. Including the bulk quadrupole contribution to SHG was crucial to accurately retrieving the RAS and to achieving fitted real and imaginary $\beta(2\omega)$ spectra consistent with a nonlinear Kramers-Kronig relation. The results demonstrate the possibility of formulating a common microscopic model of SHG and RAS responses of complicated interfaces.

DOI: 10.1103/PhysRevB.73.195330 PACS number(s): 78.68.+m, 78.40.Fy, 42.65.Ky, 42.65.An

I. INTRODUCTION

Second-harmonic generation (SHG) and reflectance-anisotropy spectroscopy (RAS) are the two dominant optical methods for noninvasive analysis of surfaces and buried interfaces. SHG is dipole forbidden in the bulk of centrosymmetric materials such as cubic elemental semiconductors; thus *p*-polarized SH signals are generated primarily within a few atomic layers of the interface or surface, where inversion symmetry is broken.[1] RAS, on the other hand, exploits the isotropy of the bulk contribution to near-normal incidence linear reflectance of cubic materials; thus reflectance anisotropies, when present, originate from lower symmetry surfaces or interfaces.[2] Theoretical methods for relating SHG and RAS responses to microscopic interface structure have advanced greatly in recent years.[3] Anisotropic interfaces of cubic materials play a critical role in achieving theoretical understanding, because they possess both SHG and RAS responses. In a few cases SHG and RAS have been calculated from a common theoretical foundation.[4] However, experimental studies that systematically compare SHG and RAS responses of the same interface are lacking. In cases where SHG has complemented RAS, it has usually been restricted to a single wavelength probe and been analyzed macroscopically using phenomenological Fourier coefficients.[5] To forge fundamental connections between SHG and RAS, both must be acquired *spectroscopically* from common samples and modeled *microscopically*.

In a previous conference proceedings paper,[6] we briefly presented a spectroscopic SHG/RAS study of native-oxidized vicinal Si(001). Cutting Si wafers vicinally at angle ζ from (001) toward the [110] direction produces an anisotropic interface, consisting of alternating terraces and step edges, that creates an RAS response, as well as onefold, twofold and threefold azimuthal anisotropies in the SHG response, that are not present at oriented Si(001)/SiO_2 interfaces.

Previously, the measured SHG spectra were analyzed phenomenologically by representing the SH field generated at each incident frequency ω by a Fourier sum[7]

$$E(2\omega)=\sum_{n=0}^{4} a_n(2\omega)\cos(n\phi), \tag{1}$$

where ϕ is the angle between the plane of incidence and the [110] direction, and each coefficient $a_n(\omega)$ is a linear combination of products of Fresnel factors and tensor components $\chi^{(2)}_{ijk}$ of the second-order nonlinear susceptibility. The main result was that the first-order step-induced coefficient $a_1(2\omega)$ spectra showed a derivativelike, ζ-dependent E_1 resonance lineshape that closely resembled the RAS spectrum, suggesting that they share a common origin in the step edges.

The present paper is devoted in part to a more complete presentation of the experimental spectroscopic SHG/RAS of the vicinal Si(001)/SiO_2 samples. In addition, instead of macroscopic phenomenological analysis, we analyze the spectra microscopically using the simplified bond-hyperpolarizability model (SBHM) introduced by Aspnes and co-workers.[8] SBHM describes the nonlinear optical response of interfaces as dipole radiation originating from the anharmonic motion of bond charges along bond directions.

SBHM is well suited for oxidized interfaces for which atomic structure varies in imprecisely known ways along the interface, because it represents the statistically averaged interfacial structure by a single tetrahedral unit and derives bond hyperpolarizabilities and angles through an empirical fitting procedure. Indeed, Aspnes and co-workers have generated accurate SBHM descriptions of the azimuthal anisotropy of SHG (Ref. 8) and fourth-harmonic[9] intensity from several oxidized Si interfaces at single, off-resonant wavelengths.

This study extends SBHM in several ways beyond previous work. First, we apply SBHM to *spectroscopic* SHG data that include a *resonant* interfacial response, in this case the resonance near the interface-modified E_1 critical point of $Si(001)/SiO_2$.[11] This procedure yields fitted complex axial hyperpolarizability spectra $\beta_{\parallel,\parallel,\parallel}(2\omega)$ (hereafter denoted $\beta^{\parallel}$) of the four tetrahedral bonds. Second, to fit SHG spectra for all vicinal angles and wavelengths, we found it necessary to allow upper bond angles to vary from perfect tetrahedral coordination. This result evidently reflects real, albeit statistically averaged, bond distortions at the Si/SiO_2 interface. Third, we extracted axial *linear* bond polarizabilities[12] $\alpha^{\parallel}(2\omega)$ from the fitted $\beta^{\parallel}(2\omega)$ using Miller's approximation[13]

$$\beta^{\parallel}(2\omega) = \Delta_{\parallel,\parallel,\parallel}\alpha^{\parallel}(2\omega)[\alpha^{\parallel}(\omega)]^2, \tag{2}$$

and used them to reconstruct the RAS data. Finally, we incorporated the bulk quadrupole contribution into the SHG analysis. This is the sole contribution to the anisotropic response of the oriented Si(001):0° surface, which therefore provides a convenient calibration of its amplitude. Its addition proved crucial in achieving fitted spectra consistent with a Kramers-Kronig relation and in successfully reconstructing RAS of the vicinal samples.

Within the same photon energy of $2.8\ \text{eV} < \hbar\omega < 3.5\ \text{eV}$, the distinct derivative feature of the experimental RAS result was successfully reproduced as well as the monotonic increase of the amplitude with the vicinal angle. Taken together, the RAS measurements and analysis demonstrate the possibility of formulating a common microscopic model of spectroscopic SHG and RAS, and motivate future studies of clean reconstructed surfaces for which atomic positions are known more precisely.

The outline of this paper is as follows. In Sec. II we describe the experimental procedures and results. Section III develops the extended simplified bond hyperpolarizability model for nonlinear and linear optical responses. This extended model is applied to and compared with the experimental measurements of SHG and RAS in Sec. IV. Relative contributions of the various bonds to the SHG/RAS responses are discussed in Sec. V. Results are summarized in Sec. VI.

II. EXPERIMENTS

A. Procedure

The Cz-grown, boron-doped (1 Ω cm) Si(001) samples were offcut at $\zeta = 0°$, 4°, 6°, 8°, and $10° \pm 0.5°$ from (001) toward the [110] crystallographic direction, producing a corrugated structure of steps and terraces. All the samples had native oxides approximately 15 Å thick.

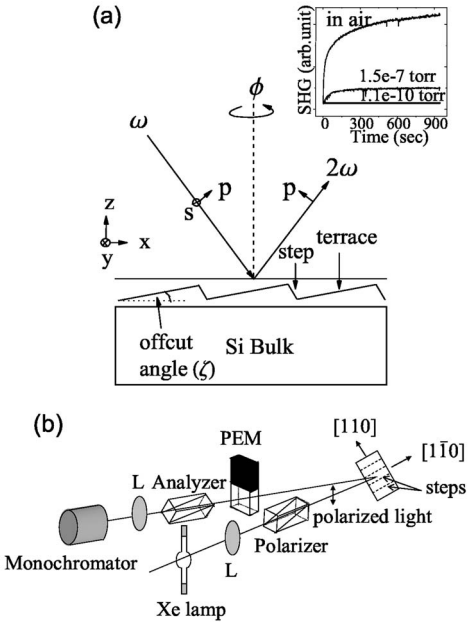

FIG. 1. Schematic of (a) SHG and (b) RAS experiments. Inset of (a) shows time-dependent SHG of vicinal $Si(001)/SiO_2$:8° for $h\nu_{SH} = 3.3$ eV, azimuth $\phi = 0°$, p-in/p-out polarization combination at three base pressures.

Figure 1(a) shows the configuration used for SHG measurements. SH signals were generated by unamplified Ti:sapphire laser pulses (~120 fs) at 76 MHz repetition rate, tunable from 900 to 720 nm ($2.8\ \text{eV} < 2\hbar\omega < 3.5\ \text{eV}$), focused unto the sample with 42° incidence angle with $\hat{\mathbf{s}}$ or $\hat{\mathbf{p}}$ polarization. Reflected $\hat{\mathbf{p}}$-polarized SH intensity was measured as a function of the azimuth ϕ at each fundamental wavelength at increments of 10 nm within the tuning range. The plane of incidence was along [110] at $\phi = 0°$. All SHG data were normalized to reference SHG from a z-cut quartz wedge to correct for variations in intensity and pulse structure of the incident laser during tuning.

Accumulation of laser-induced charge on the oxide surface can cause time-dependent electric-field-induced SHG during data acquisition, as shown in the inset of Fig. 1(a) for vicinal $Si(001)/SiO_2$:8° at $2h\nu_{SH} = 3.3$ eV. This effect is caused by multiphoton excitation of electrons from the Si valence band to the oxide conduction band, initiating their slow diffusion to oxide surface traps.[14] Since charge builds up on the same time scale as a sample rotation or a spectral scan, it was essential to suppress this effect to avoid introducing artifacts into the azimuthal—or spectral dependence of SHG. We accomplished this in part by reducing ambient pressure, as illustrated in the inset of Fig. 1(a), thereby suppressing the catalytic role of ambient oxygen in the charging process.[14] Significant time-dependent SHG persisted down to 10^{-8} Torr, but almost completely disappeared at 10^{-10} Torr. Thus, all SHG data were acquired in UHV at base pressure 10^{-10} Torr. We further suppressed the effect by displacing the focused laser spot slightly from the sample rotation axis, so that its movement prevented charge buildup over time.

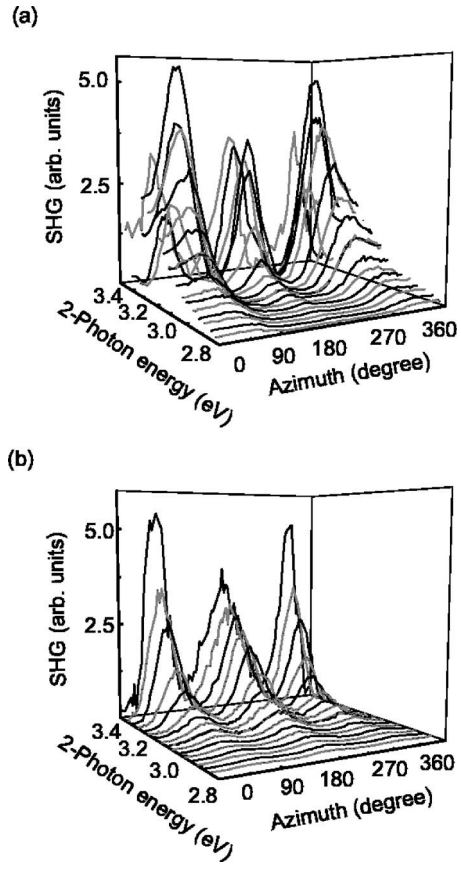

FIG. 2. SHG intensity as a function of azimuth ϕ and photon energy for $Si(001)/SiO_2:10°$ with polarization combinations (a) p-in/p-out and (b) s-in/p-out.

RAS data were acquired from the same samples in air over a spectral range $1.5<\hbar\omega<4.6$ eV. Collimated white light from a Xe arc lamp reflected from the sample, incident as near to normal ($\theta_i=5°$) as possible while avoiding overlap of incident and reflected beams. The incident field was polarized 45°(or 135°) to the step edges. The reflected light was phase-modulated photoelastically at $\omega_{mod}=50$ kHz, polarization analyzed, then spectrally analyzed by a monochromator [see Fig. 1(b)]. The ω_{mod} and $2\omega_{mod}$ components of the detected intensity are related to the imaginary and real part, respectively, of the complex anisotropy $\Delta r/r=2(r_{\parallel}-r_{\perp})/(r_{\parallel}+r_{\perp})$, where $r_{\perp}$ and $r_{\parallel}$ are the complex reflectance for light polarized along the $\perp=[110]$ and $\parallel=[1\bar{1}0]$ principal axes, respectively.[15] RAS was acquired at two fixed azimuths, $\phi=45°$ and 135°, to confirm internal consistency of the data.

B. Results

Figure 2 illustrates the complete normalized azimuthal and spectral dependence of SHG from the $Si(001)/SiO_2:10°$ sample for (a) p-in/p-out and (b) s-in/p-out polarization combinations. A similar set of data was acquired for each sample. The azimuthal-dependence shows strong onefold and threefold anisotropies. The increase in SHG intensity near 3.3 eV results from the interface-modified E_1 critical point resonance.

Figure 3 shows how the rotational anisotropy of SHG varies with vicinal angle ζ for a SH photon energy (2.85 eV) that is well below resonance (left column) and two SH photon energies (3.31 and 3.44 eV) that are near the E_1 resonance (center and right columns). The vertical scales of Figs. 2 and 3 are internally consistent. For the $\zeta=0°$ sample, only

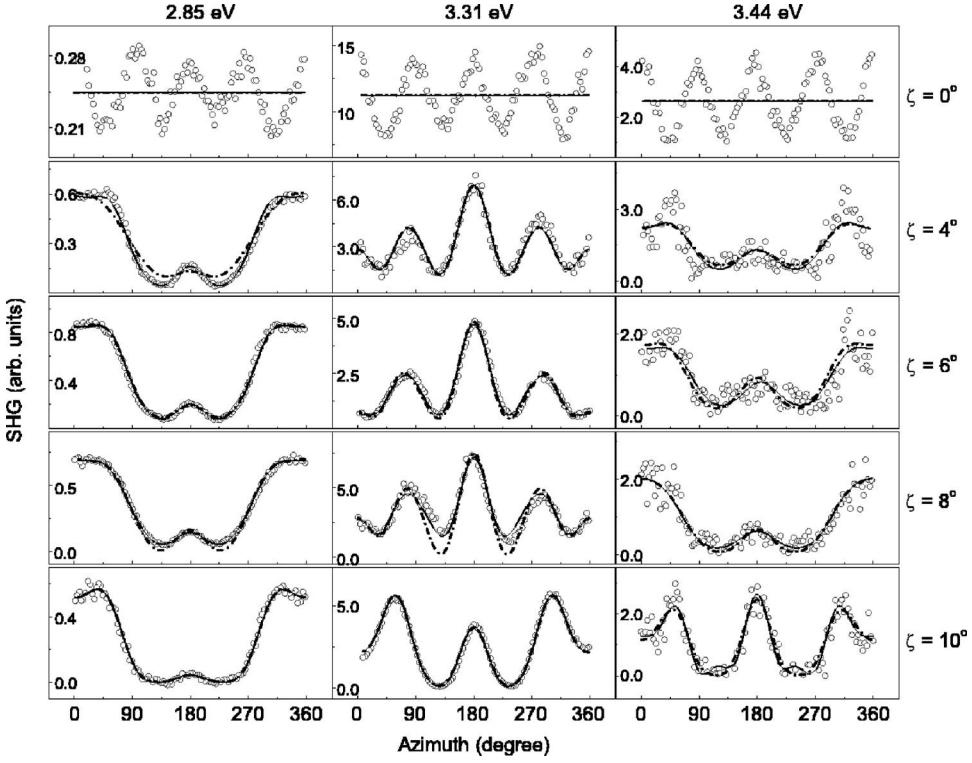

FIG. 3. Rotational anisotropy of p-in/p-out SHG for offcut angles 0°, 4°, 6°, 8°, and 10° for SH photon energies 2.85 eV (left column), 3.31 eV (middle column), and 3.44 eV (right column). Curves are fits to the SBHM using an ideal tetrahedron (dash-dot) or tetrahedron with variable upper bond angles (solid line). These fits are done using SBHM which includes the interface dipole effect only, without considering the contribution from the bulk. Note for the 0° sample in the first row, the interface dipole contribution to the SH radiation gives isotropic responses, unable to represent the fourfold anisotropy whose sole contribution comes from the bulk quadrupole.

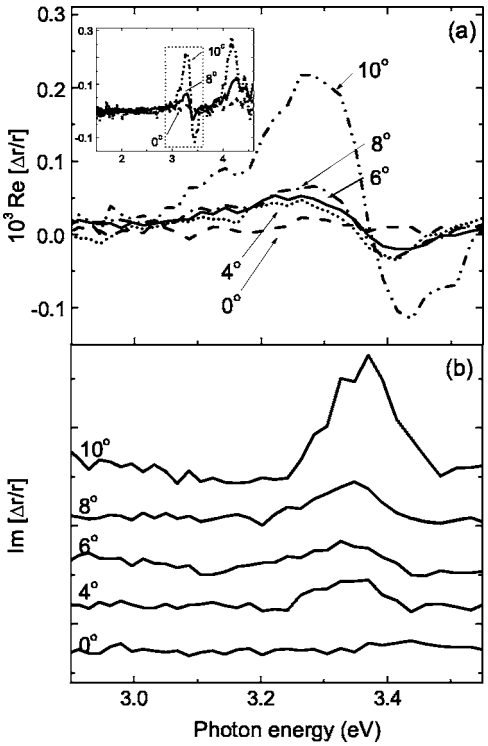

FIG. 4. Normalized (a) real and (b) imaginary parts of the RAS of native-oxidized vicinal Si(001) at five off-cut angles $\zeta=0°,4°,6°,8°,10°$ for a photon energy range $2.8<h\nu<3.6$ eV that corresponds to the SHG tuning range. The inset in (a) shows the complete Re$[\Delta r/r]$ spectra from 1.5 to 4.6 eV for three off-cut angles.

isotropic and fourfold anisotropic contributions are present, consistent with the macroscopic C_{4v} symmetry of the Si(001) surface. As ζ increases, additional step-induced onefold and threefold anisotropies emerge, consistent with the macroscopic C_{1v} symmetry of the stepped surface.[7] These step-induced anisotropies also depend strongly on frequency, as seen by comparing the 3.31 eV (3.44 eV) at the center column (right column) to the 2.85 eV data at the left column.

Figure 4 shows the (a) real and (b) imaginary components of a portion of the RAS within a photon energy range of $2.8<h\nu<3.6$ eV near the E_1 critical point that corresponds to the range of $h\nu_{\mathrm{SH}}$ in the SHG measurements. The inset of Fig. 4(a) shows the real part of several RAS over a wider range $1.5<h\nu<5$ eV. A ζ-dependent E_2 feature is evident at $h\nu\approx4.2$ eV. The spectra are featureless below 2.8 eV.

The features in the main panels of Fig. 4 grow monotonically with ζ, and vanish for $\zeta=0°$, confirming that they originate from the step edges. The Re$[\Delta r/r]$ curves near E_1 [Fig. 4(a)] are similar in shape to the derivative dR/dE of the reflectance spectrum $R(E)$ of silicon. This shape suggests that the E_1 gap along the [110] direction (i.e., $\perp$ to the step edges) is slightly lower in energy than along the $[1\bar{1}0]$ direction (i.e., $\parallel$ to the step edges). Similarly Im$[\Delta r/r]$ [Fig. 4(b)] resembles the difference between two slightly shifted spectra of the reflective phase across the E_1 gap. As expected from this interpretation, its peak coincides with the zero crossing of Re$[\Delta r/r]$.

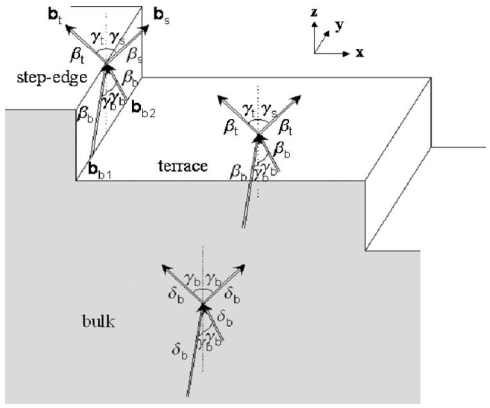

FIG. 5. Step-edge and terrace bonds of the tetrahedra representing the Si/SiO_2 interface and the bulk tetrahedron.

III. SIMPLIFIED BOND MODEL

Interpretation of SHG data such as Figs. 2 and 3 is usually limited to a discussion of the contribution of various tensor components of the second-order susceptibility $\chi^{(2)}_{ijk}$, determined from purely phenomenological analysis.[7] Recently considerable progress has been made in interpreting experimental SHG spectra from well-characterized surfaces with small unit cells using first-principles band structure calculations, although the calculations remain difficult and the agreement qualitative.[3] Bond-hyperpolarizability models have emerged as an intermediate approach that permits SHG data to be interpreted directly in terms of the microscopic properties of a few individual bonds that are fitted empirically. In covalent semiconductors, mobile bond charge provides the polarizable unit. The SHG signal is interpreted as the far-field intensity of the square of the superposition of fields radiated by the anharmonic component of the bond charge motion. The linear response consists of radiation from the harmonic component of bond charge motion.

A. Tetrahedral bond structure

Previous SBHM analyses represented the nonlinear optical response of the $Si(001)/SiO_2$ interface by a single tetrahedron of polarizable Si-Si bonds, all making the same angle $\gamma_b=\sin^{-1}(\sqrt{2/3})=54.736°$ with the z axis, as occurs in bulk Si.[8,9] Our analysis of vicinal $Si(001)/SiO_2$ also began from this point, but did not yield satisfactory fits to the SHG data at all wavelengths. To improve fits to the data, we introduce up to three conceptually distinct tetrahedral polarizable-bond units, as illustrated in Fig. 5. Separate tetrahedra represent the step-edge and terrace responses. Together these are responsible for the interface dipolar SHG response. A third tetrahedron just beneath the interface was introduced to represent the bulk quadrupole SHG response. Only for this bulk tetrahedron were all four bond angles fixed *a priori* at $\gamma_b=54.736°$, and all four bonds assigned the same complex hyperpolarizability δ_j, which is quadrupolar in bulk Si.

For the interfacial units, the two lower "back" bonds lie along the unit vectors

$$\hat{\mathbf{b}}_{b1,b2} = \pm \sin(\gamma_b)\hat{\mathbf{y}} + \cos(\gamma_b)\hat{\mathbf{z}} \quad (3)$$

in the yz plane, parallel to the step edges. From symmetry, the two back bonds make the same angle γ_b with the z axis and have identical dipolar hyperpolarizabilities β_b and linear polarizabilities α_b. In addition, because backbonds are relatively rigid and bulklike,[18] γ_b was held fixed at the ideal bulk tetrahedral value 54.736° for both interfacial tetrahedra in all fits. For further simplification, and to restrict the number of fitting parameters, β_b and α_b of the backbonds were assumed to be identical in the step-edge and terrace tetrahedra. Moreover β_b and α_b were initially taken as real numbers. This is always possible for one bond in each tetrahedron, since only relative phases among the β_j and α_j are needed for modeling measurements of SHG amplitude. After the fit, all β_j were multiplied by a common frequency-dependent phase factor $e^{-i\varphi(\omega)}$ that was chosen to enforce a Kramers-Kronig relation between real and imaginary β_b of the backbonds as discussed further below. Since the phase factor is common to all four bonds, it does not affect the fit to the data.

Variations from bulk tetrahedral symmetry were allowed in the upper bonds. Soft interfacial Si-O-Si bridge bonds allow much greater flexibility in these bond angles.[18] For the step-edge tetrahedron, the axes of the two upper Si-O bonds are described by unit vectors

$$\hat{\mathbf{b}}_{s,t} = \pm \sin(\gamma_{s,t})\hat{\mathbf{x}} + \cos(\gamma_{s,t})\hat{\mathbf{z}} \quad (4)$$

lying in the xz plane, perpendicular to the y-directed step edges. They point into the SiO_2 layer, are tilted either over the step (s) or back toward the upper terrace (t) and make angles γ_s or γ_t, respectively, with the z axis. The upper bonds have complex hyperpolarizabilities β_s and β_t and linear polarizabilities α_s and α_t. A corresponding set of γ_j, β_j and α_j describe the upper bonds of the terrace tetrahedron, and in principle are independent of the step-edge values. In practice, however, simplifications were required here, also, to avoid a proliferation of fitting parameters that provided little physical insight. *Ab initio* calculations show that soft interfacial Si-O-Si bridge bonds give rise to a broad distribution $90° \leqslant \gamma_s + \gamma_t \leqslant 140°$ of interfacial O-Si-O bond angles,[18] in contrast to the more rigid Si-Si back and bulk bonds. Therefore, with regard to upper bond angles little physical insight is gained by maintaining distinct angles in these two interfacial tetrahedra. Thus, we used only a *single pair* of upper bond angles γ_s and γ_t as fitting parameters applying to both tetrahedra, with the understanding that they represent statistical averages. Since the step-edge and terrace tetrahedra thereby have identical structures, they can, for purposes of fitting data, be merged into a single tetrahedron in which the effective hyperpolarizability β_j of bond $\hat{\mathbf{b}}_j$ is a weighted sum[20]

$$\beta_j = \beta_j^{\text{step}} \tan\zeta + \beta_j^{\text{terrace}}(1 - \tan\zeta) \quad (5)$$

of step and terrace contributions, where $\tan\zeta$ is proportional to the step density. Here, the two upper bonds $\hat{\mathbf{b}}_{s,t}$ in the terrace site are assumed to share the same hyperpolarizability with $\hat{\mathbf{b}}_t$ of the step edge; i.e., $\beta_s^{\text{terrace}} = \beta_t^{\text{terrace}} = \beta_t^{\text{step}}$. A similar expression applies to the effective α_j. For the back bonds, Eq. (5) yields simply β_b.

B. Second-harmonic response

The SH polarization density $\mathbf{P}^{(2)}$ is the sum

$$\mathbf{P}^{(2)} = \frac{1}{V}\sum_{n=1}^{N}\sum_j \mathbf{p}_j^{(2),n} \quad (6)$$

of the SH dipole moments $\mathbf{p}_j^{(2)}$ of the individual bonds ($1 < j < 4$) of the nth tetrahedron, where V is the unit cell volume. The dominant contribution to $\mathbf{P}^{(2)}$, and the only one considered in previous SBHM analyses,[8,9] arises from charge motion parallel to the axes $\hat{\mathbf{b}}_j$ of the interfacial bonds, and is written

$$\mathbf{P}^{(2),\text{int}} = \frac{1}{V}\sum_j \mathbf{p}_j^{(2),\text{int}} = \frac{1}{V}\sum_j (\beta_j^{\parallel}\hat{\mathbf{b}}_j\hat{\mathbf{b}}_j\hat{\mathbf{b}}_j) \cdot \mathbf{EE}, \quad (7)$$

where $\mathbf{E}$ is the incident optical field, and the sum runs over the four bonds of the effective interfacial tetrahedron. Local field variations in $\mathbf{E}$ among the bonds, caused by contributions from neighboring induced dipoles, are not included explicitly, but are incorporated into the hyperpolarizabilities $\beta^{\parallel}$.

As an extension of the model, we also considered the transverse interfacial polarization density

$$\mathbf{P}_{\perp}^{(2),\text{int}} = \frac{1}{V}\sum_j (\beta_j^{\perp}\hat{\mathbf{b}}_j^{\perp}\hat{\mathbf{b}}_j\hat{\mathbf{b}}_j^{\perp}) \cdot \mathbf{EE}, \quad (8)$$

where $\hat{\mathbf{b}}_j^{\perp} = [\mathbf{E} - \hat{\mathbf{b}}_j(\hat{\mathbf{b}}_j \cdot \mathbf{E})]/\sqrt{1-(\mathbf{b}_j \cdot \mathbf{E})^2}$ is a unit vector perpendicular to the bond direction.

As an alternative correction to $\mathbf{P}_{\parallel}^{(2),\text{int}}$, we considered an additional quadrupolar SH source term

$$\mathbf{P}_Q^{(2),\text{bulk}} = \frac{1}{V}\sum_j (\delta_b^{\parallel}\hat{\mathbf{b}}_j\hat{\mathbf{b}}_j\hat{\mathbf{b}}_j\hat{\mathbf{b}}_j) \cdot \mathbf{E}_b\boldsymbol{\nabla}_b\mathbf{E}_b, \quad (9)$$

where $\delta_b^{\parallel}$ is the bulk quadrupolar hyperpolarizability originating from the fully symmetric bulk Si tetrahedron. For simplicity, only axial charge motion was considered in describing $\mathbf{P}_Q^{(2),\text{bulk}}$ and all the bulk bonds share the common $\delta_b^{\parallel}$. Details of the procedure for introducing the corrections (8) and (9) are described in the data analysis in Sec. IV.

The far-field SH radiation from the SH dipoles is[8,9]

$$\mathbf{E}_{\text{ff}}^{2\omega} = \frac{k^2 e^{ikr}}{r}[\hat{I} - \hat{k}\hat{k}] \cdot \sum_{n=1}^{N}\sum_j \mathbf{p}_j^{(2),n}, \quad (10)$$

where $\hat{I}$ is the unit tensor and $\hat{k}$ is a unit vector in the direction of the observer. For observation angle θ_o, $\hat{k} = -\hat{\mathbf{x}}\sin\theta_o + \hat{\mathbf{z}}\cos\theta_o$. For incidence angle θ_i, the $\hat{\mathbf{s}}$-polorized and $\hat{\mathbf{p}}$-polarized incident electric fields are $\mathbf{E}_s = E_s\hat{\mathbf{y}}$, and $\mathbf{E}_p = E_p(-\hat{\mathbf{x}}\cos\theta_i + \hat{\mathbf{z}}\sin\theta_i)$. The θ_i and θ_o used in the calculation were not the laboratory angle 42°, but propagation angles inside the material determined by refraction. For calculations involving the interface tetrahedron, angles inside the SiO_2 layer ($\theta_{i,\text{int}} = 27.4°$ and $\theta_{o,\text{int}} = 27.1°$), after taking into account refraction from the air-SiO_2 interface, were used. The dispersion of these angles for the wavelength range used in this study was negligible. Since the backbonds of the interface tetrahedron could be considered to lie below

the SiO_2-Si interface, the possibility arises that θ_i and θ_o for these bonds should take into account the additional refraction. However, we found that this assumption degraded the fit quality. It was, therefore, not considered further. On the other hand, when the quadrupolar contribution [Eq. (9)] was included in the calculation, propagation angles inside the Si substrate were used. Dispersion of the incidence angle was still small, so the average value over the range 720 nm $<\lambda<$ 900 nm ($\theta_{i,\mathrm{bulk}}=10.5°$) was used. The bulk observation angle $\theta_{o,\mathrm{bulk}}$, on the other hand, varies from 4.5° to 8.1° because of the high dispersion of silicon at the SH frequency. Thus, the frequency dependence of $\theta_{o,\mathrm{int}}$ was retained explicitly in calculations using Eq. (9).

C. Linear response

The linear polarization density $\mathbf{P}^{(1)}$ is the sum

$$\mathbf{P}^{(1)}=\frac{1}{V}\sum_j \mathbf{p}_j^{(1)}=\frac{1}{V}\sum_j [(\alpha_j^{\parallel}\hat{\mathbf{b}}_j\hat{\mathbf{b}}_j)\mathbf{E}+(\alpha_j^{\perp}\hat{\mathbf{b}}_j^{\perp}\hat{\mathbf{b}}_j^{\perp})\mathbf{E}], \tag{11}$$

where we have included both axial ($\alpha_j^{\parallel}$) and transverse ($\alpha_j^{\perp}$) bond polarizabilities. Formal inclusion of the latter was motivated by the conclusion of previous bond-(hyper)polarizability models[10,12] that transverse charge motion contributes more strongly to the linear than to the second-order nonlinear optical response of tetrahedrally coordinated semiconductors.

To calculate RAS, the experimental incidence angle $\theta_i=5°$, $\hat{\mathbf{s}}$-polarized incident field and azimuth $\phi=45°,135°$ were used. The $\hat{\mathbf{x}}$ component of the reflected beam is then equivalent to the RAS between the light polarized along the $[1\bar{1}0]$ and [110] principal axes. Since this RAS response originates entirely from the interface, only interfacial bonds $\hat{\mathbf{b}}_j$ [Eqs. (3) and (4)] were used in evaluating the sum. The anisotropic component of the far-field radiation pattern is then

$$\mathbf{E}_{\mathrm{ff}}^{\omega}=\frac{k^2e^{ikr}}{r}[\hat{I}-\hat{k}\hat{k}]\cdot\sum_j \mathbf{p}_j^{(1)}. \tag{12}$$

We *reconstructed* the RAS using Eq. (12), with parameters derived from the SHG fit as follows. Interfacial bond angles $\gamma_{s,t,b}$ were imported without change. The longitudinal linear polarizabilities $\alpha_j^{\parallel}(\omega)$ were derived from the hyperpolarizabilities $\beta_j^{\parallel}(\omega)$ using Miller's approximation defined in Eq. (2). For $720<\lambda<900$ nm, the polarizability $\alpha_j^{\parallel}(\omega)$ at the fundamental photon energy can be considered constant. Then Eq. (2) simplifies to $\beta_j^{\parallel}(2\omega)=g_j^{\parallel}\alpha_j^{\parallel}(2\omega)$, where $g_j^{\parallel}=\Delta_j^{\parallel,\parallel,\parallel}[\alpha_j^{\parallel}(\omega)]^2$. In principle, the transverse polarizability could be derived similarly using $\beta_j^{\perp}(w\omega)=g_j^{\perp}\alpha_j^{\perp}(2\omega)$, where $g_j^{\perp}=\Delta_j^{\perp,\parallel,\perp}\alpha_j^{\parallel}(\omega)\alpha_j^{\perp}(\omega)$. However, the ratio $g_j^{\parallel}/g_j^{\perp}$ is left undetermined. Moreover, $\beta^{\perp}$ is determined less accurately than $\beta^{\parallel}$ from the SHG fit. A better algorithm for introducing $\alpha^{\perp}$ is based on the generalized Clausius-Mossotti (CM) relation $\chi=(16/3a^3)(\alpha^{\parallel}+2\alpha^{\perp})$, where a is the lattice constant. In the bulk crystal, CM relates $\alpha^{\perp}$ analytically to $\alpha^{\parallel}$ via the measured dielectric function $\epsilon=1+4\pi\chi$. For the bulklike interfacial backbonds, this relation provides a reasonable approximation, and was therefore used to approximate $\alpha_b^{\perp}$ in those bonds. In the upper (s,t) bonds, the bulk ϵ is no longer meaningful. In the RAS reconstructions presented here, the ratio $\alpha_{s,t}^{\perp}/\alpha_{s,t}^{\parallel}$ was fixed at the same value as $\alpha_b^{\perp}/\alpha_b^{\parallel}$ in the backbonds. This choice is arbitrary, but the spectral structure and ζ dependence of reconstructed RAS—the key features that were compared with data—proved insensitive to it. As discussed in Sec. IV, these features were determined almost entirely by the $\alpha_j^{\parallel}$. The main effect of including $\alpha_j^{\perp}$ was to adjust the overall amplitude of Re $\Delta r/r$. The absolute amplitude of Re $\Delta r/r$ also depends on the prefactors $g_j^{\parallel,\perp}$, and our model provides no algorithm for isolating the role of $\alpha_j^{\perp}$. Instead we reconstructed RAS data using a single overall scaling factor. Thus, the transverse bond hyperpolarizabilities are incorporated according to the above algorithm to exhibit qualitatively their effect on reconstructed RAS, but should not be construed as a quantitative extraction of their values.

D. Nonlinear Kramers-Kronig relations

Since our SHG data is spectroscopic, we checked whether the empirically fitted hyperpolarizability spectra were consistent with standard nonlinear optical Kramers-Kronig (KK) relations.[16,17] This important constraint on fitted parameter values cannot be applied to single wavelength SHG data. Since SHG spectra were acquired only over a 0.6 eV spectral range, an algorithm is needed to approximate spectral dependence outside this range so that KK integrals can be evaluated over infinite limits. This was handled by treating the resonances of Im$[\beta]$ as positive Lorentzian functions, which have well-defined asymptotic behavior outside the experimental range. We began the analysis by explicitly enforcing a nonlinear KK relation between Im$[\beta_b]$ and Re$[\beta_b]$ of the backbonds, where initially we had assumed Im$[\beta_b]=0$ to facilitate empirical fits to SHG data. For a simple, qualitative KK analysis, Im$[\beta_b]$ was modeled as a single Lorentzian resonance at the E_1 energy. The oscillator strength and width of the Lorentzian were varied to achieve the best fit to Re$[\beta_b]$, preserving the fitted $|\beta_b|$ at each frequency. The remaining complex bond hyperpolarizabilities were then shifted in phase at each frequency by the same amount required to enforce a KK relation in the backbonds, thereby preserving relative phases among the β_j and leaving the original empirical fit unaltered. We then evaluated the resulting Im$[\beta_{s,t}]$ and Re$[\beta_{s,t}]$ spectra qualitatively for consistency with nonlinear KK relations.[16,17]

Use of a single E_1-like Lorentzian resonance in Im$[\beta]$ neglects the possibly significant impact of higher energy resonances on Re$[\beta]$ within the experimental spectral range. However, higher energy resonances contribute a featureless positive background to Re$[\beta]$ within this range, whereas the E_1 resonance contributes the distinctive rapidly varying component (i.e., positive/negative at frequencies above/below the E_1 resonance) of Re$[\beta]$. Thus, for qualitative KK analysis, the single-resonance approximation is acceptable as long as judgment is based on conjunction of a qualitatively correct dispersive line shape in Re$[\beta]$ (independent of background) and a positive E_1-like resonance in Im$[\beta]$. To improve upon

this simple analysis, we also performed a two-resonance KK analysis of the β_j spectra obtained from our final SHG fit. An E_2-like resonance of adjustable strength and width was included to approximate the effect of higher energy resonances. Not surprisingly, in view of the additional parameters, a more accurate KK relation between Im[β] and Re[β] could be achieved for all bonds. The greatest improvement occurred in modeling Re[β] just above the E_1 resonance, where the E_1 and higher energy resonances of Im[β] make contributions of opposite sign to Re[β].

IV. DATA ANALYSIS

Here we describe the result of fits of increasing sophistication applied to the *p*-in/*p*-out SHG data. These yield hyperpolarizability spectra of each interfacial and bulk bond. Then we present our reconstruction of the RAS data based on the extracted SHG parameters, comparing them to the experimental results. We also reconstruct *s*-in/*p*-out SHG data using the same fitting parameters from the *p*-in/*p*-out as a crosscheck.

A. SBHM with rigid interface tetrahedron

For initial fits of *p*-in/*p*-out SHG, we use only a single interface tetrahedron with all bond angles fixed at the bulk value $\gamma_b = \sin^{-1}(\sqrt{2/3}) = 54.736°$. The SH polarization is then calculated from Eq. (7), with complex axial bond hyperpolarizabilities $\beta^{\parallel}_{s,t}$ and a real $\beta^{\parallel}_b$ shared by the two backbonds as the only free parameters. The vicinal angles were fixed at their nominal values. The incidence angle was also fixed after refraction within the SiO_2 was taken into account. The dash-dot curves in Fig. 3 show selected results of this fit at each ζ for three SH photon energies. For $\zeta = 0°$ the interface SHG dipolar response is isotropic. Hence, the fitted curves are simply horizontal lines that do not reflect the observed fourfold anisotropy, because it is of bulk quadrupole origin. For nonzero ζ, the strong anisotropy from the step edge evidently dominates over the bulk quadrupolar anisotropy, because we find that the simple rigid interface tetrahedron model, neglecting bulk contribution, fits the main qualitative features of observed SHG anisotropy at most wavelengths reasonably well (see Fig. 3). Nevertheless, there are three difficulties with this simple model. First, it leads to an inconsistency with the KK relation between real and imaginary $\beta_{s,t}$. This issue is discussed at the end of Sec. IV B below. Second, it leads to a poor reconstruction of RAS data. This issue is discussed in Sec. IV C below. Third, significant quantitative discrepancies remain in some cases. Some examples are evident in Fig. 3 (for example, $\zeta = 4°$, 2.85 eV and $\zeta = 8°$, 3.31 eV). Before discussing the first two issues, we first show that quantitative fits to the SHG data for nonzero ζ can be improved significantly with a slight modification of the rigid tetrahedron model.

B. SBHM with flexible interface tetrahedron

As a first step to improve the fits, we allowed for the flexibility of Si-O-Si bridge bonds by allowing the upper bond angles $\gamma_{s,t}$ of the single tetrahedron to vary as free parameters along with the $\beta^{\parallel}_j$. Initially γ_s and γ_t were allowed to vary for each wavelength, even though they do not depend on wavelength. We found that, for each ζ, the fitted $\gamma_{s,t}$ never varied by more than ±3.3% with wavelength. This crosscheck indicates that the fitted $\gamma_{s,t}$ reflect real interfacial structure, rather than artificial compensation for errors in the fit. The average fitted $\gamma^{\zeta}_{s,t}$ for each ζ, presented in the Table I, deviate significantly from the ideal bulk angle 54.736°. A second fit was then performed in which $\gamma_{s,t}$ were held fixed at these average values for each ζ. Some examples of this fit are shown as solid curves in Fig. 3. The discrepancy between the fit and the experiments was minimized, producing an overall excellent fit.

TABLE I. Fitted average upper bond angles γ_s, γ_t at each vicinal angle ζ. Only axial interfacial bond hyperpolarizabilities $\beta^{\parallel}_j$ were included in the fit.

ζ	4°	6°	8°	10°
γ_s	45.5° ± 1.4°	51.0° ± 3.2°	63.5° ± 4.1°	47.8° ± 1.3°
γ_t	44.8° ± 3.6°	38.9° ± 5.7°	31.3° ± 0.8°	37.5° ± 4.2°

For all vicinal angle, the fitted average γ_s and γ_t in Table I are close to the average of the wide distribution of O-Si-O bond angles ($90° \leqslant \gamma_s + \gamma_t \leqslant 140°$) found in first principles calculations of planar Si/SiO_2 interfaces.[18] The step bond angle γ_s increases with the vicinal angle between 4° and 8° while the terrace bond angle γ_t decreases. On the other hand, the fitted $\gamma_{s,t}$ for $\zeta = 10°$ does not follow this trend. The fitted hyperpolarizabilities of the $\zeta = 10°$ sample show a similar discontinuity in the ζ trend. It may reflect faceting which is known to occur for $\zeta > 9°$.[19] Thus, the anomalous parameters at $\zeta = 10°$ may result from orientational averaging.

Figure 6 shows the fitted spectra of the axial hyperpolarizabilities. With regard to the real parts of β_j {see left column in Fig. 6, the step bond β_s [panel (a)] and terrace bond β_t [panel (c)]} show the most variation with vicinal angle. This sensitivity to ζ stems from the exposure of the upper bonds to the changing interface environment. The backbond β_b [panel (e)], by contrast, are almost completely insensitive to vicinal angle, except for $\zeta = 10°$. Evidently, these lower bonds are relatively shielded from ζ-dependent interface changes.

A nonlinear KK relation was explicitly enforced between Im[β_b] [panel (f)] and Re[β_b] [panel (e)]. Specifically, Im[β_b] is positive at all ω with a peak at around $\hbar\omega \simeq 3.4$ eV that corresponds to the zero crossing of Re[β_b]. This simple fit, however, yields Im[β_s] [panel (b)] and Im[β_t] [panel (d)] that are, in general, inconsistent with a nonlinear KK relation with their corresponding real spectra. For example, Im[β_t] are mostly flat except for $\zeta = 8°$ over the whole spectroscopic range, and in some cases negative. This inconsistency with the KK relation suggests the inadequacy of the SBHM that only takes the interface bond contribution into account.

C. RAS reconstruction: Initial attempt

Despite the unphysical features of these β_j we attempted to reconstruct the RAS data in Fig. 4(a) using them as input

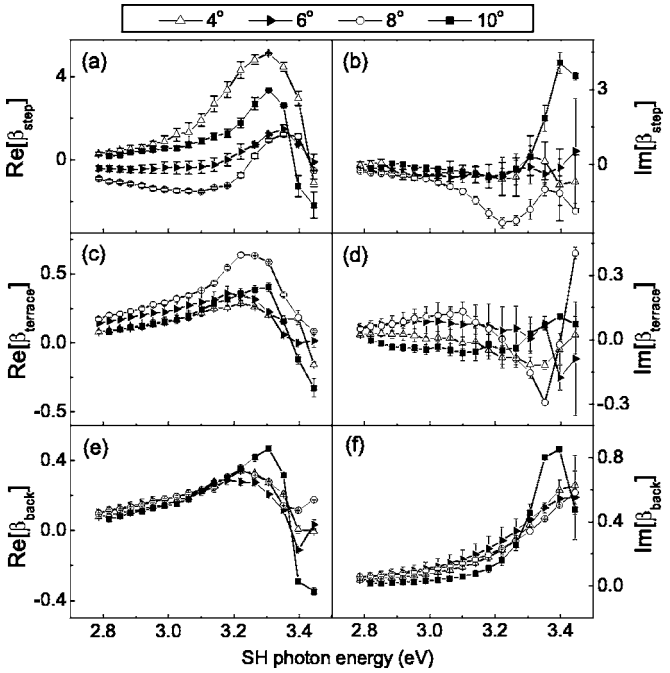

FIG. 6. Spectroscopy of the axial hyperpolarizabilities at each vicinal angle. The left column presents the real and the left column imaginary values of the complex β_j. The imaginary part of the backbond hyperpolarizability $\mathrm{Im}[\beta_{\mathrm{back}}]$ (f) was produced out of the $\mathrm{Re}[\beta_{\mathrm{back}}]$ through Kramers-Kronig relations. Error bars are correlated with uncertainty ranges in Table I.

parameters. The axial and transverse linear polarizabilities $\alpha_j^{\parallel,\perp}$ were approximated using the algorithms described in Sec. III C. Figure 7 shows reconstructed RAS using $\alpha_j^{\parallel}$ derived from $\beta_j^{\parallel}$ via Miller's approximation. In general, the reconstructed RAS in Fig. 7 poorly reproduce the derivative-like spectral structure observed near the E_1 critical point. This spectral shape is determined almost entirely by the $\alpha_j^{\parallel}$. The $\alpha_j^{\perp}$ influence RAS amplitude, but affect the spectral shape minimally. This is demonstrated explicitly by insets that show examples of $\mathrm{Re}[\Delta r/r]$ reconstructed using the $\alpha_j^{\parallel}$ only. Compared with the corresponding main panels, all

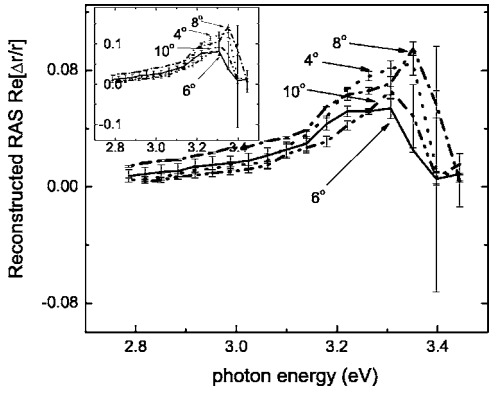

FIG. 7. Reconstructed RAS using the axial linear polarizabilities $\alpha_j^{\parallel}$ derived from fitted $\beta_j^{\parallel}$ in Fig. 6 and $\alpha_j^{\perp}$ derived from the Clausius-Mossotti relation. The inset is the RAS reconstruction with the axial $\alpha_j^{\parallel}$ only.

spectral features were preserved except RAS amplitude.

The greatest discrepancy can be found in the lack of the correlation between the vicinal angle and the overall amplitude $|\mathrm{Re}[\Delta r/r]|_{\max}$ of the RAS. The measured $|\mathrm{Re}[\Delta r/r]|_{\max}$ increases monotonically with ζ, whereas the reconstructed RAS does not.

As an alternative way to incorporate the transverse linear polarizability $\alpha^{\perp}$ contribution to the RAS, we extended the SHG fit in such a way that it includes not only the axial but also the transverse hyperpolarizability $\beta^{\perp}$ [Eq. (8)]. In order to suppress the proliferation of the free parameters in the calculation, only two upper interfacial bonds were assigned real transverse hyperpolarizabilities $\beta_{s,t}^{\perp}$. In this fit, the backbond $\beta_b^{\parallel}$ [Fig. 6(e)] and the same bond angles (Table I) from the previous fit were imported, leaving thereby only axial and transverse hyperpolarizabilities of the upper interfacial bonds as free parameters. This incorporation of the transverse hyperpolarizability in the SHG fit gives us a new set of linear axial and transverse polarizabilities $\alpha^{\parallel,\perp}$. But RAS reproduced in this way showed greater discrepancy with the experimental results.

D. SBHM with bulk quadrupole contribution

Finally, we included the bulk quadrupolar contribution [Eq. (9)] in the simplified bond model. Each bond of the bulk tetrahedron (Fig. 5) was assigned an equivalent complex axial quadrupolar hyperpolarizability $\delta^{\parallel}$. Far-field SH radiation E_{ff} in Eq. (10), for p-in/p-out polarization configuration can be written

$$\mathbf{E}_{\mathrm{ff}}^{2\omega} = \hat{\mathbf{x}}E_{\mathrm{int},x} + \hat{\mathbf{z}}E_{\mathrm{int},z} + Fe^{i\phi_F}(\hat{\mathbf{x}}E_{\mathrm{bulk},x} + \hat{\mathbf{z}}E_{\mathrm{bulk},z}), \quad (13)$$

where $E_{\mathrm{int(bulk)},j}$ $(j=x,z)$ is the SH generated from the interfacial (bulk) dipolar (quadrupolar) contribution in the j-polarized direction and F and ϕ are, respectively, the Fresnel amplitude and phase based on the SH boundary condition.[21]

This can be done without increasing the number of free parameters by utilizing the Si(001):0° SH data. The fourfold anisotropy of the oriented Si(001):0° interface has the bulk as its sole origin. The SBHM developed with the interface dipolar contribution produces the isotropic response shown in Fig. 3. But when we incorporated the bulk quadrupole contribution of Eq. (9) in the SH far field radiation, the anisotropic response of the Si(001):0° interface is fitted nicely as shown in Fig. 8. Spectra of the quadrupolar hyperpolarizability $\delta_b^{\parallel}$ are thereby generated.

The fit was accomplished on Si(001):0° with all bond angles of the bulk tetrahedron fixed at 54.736°. Since the dependence of the bulk contribution on the vicinal angle[7] can be considered small for $\zeta \leqslant 10°$, these $\delta_b^{\parallel}$'s from Si(001):0° were applied to the SHG fitting procedure for the vicinal samples. The new set of bond angles and the $\beta_j^{\parallel}$ and $\delta^{\parallel}$ spectra resulting from this fit are shown in Table II and Fig. 9, respectively.

The bond angles $\gamma_{s,t}$ in Table II follow almost the same trend as in Table I; i.e., step bond angle γ_s increases and terrace γ_s decreases with the vicinal angle between 4° and 8°. Within error bars, the fitted $\gamma_{s,t}$ lie within the bond angle

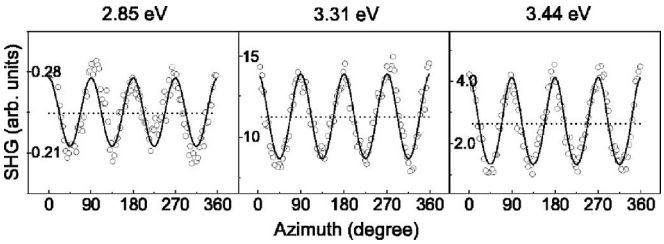

FIG. 8. Same as the first row of Fig. 3 for Si/SiO_2:0° SHG experimental data at three different SH photon energy. The dotted lines are the fits to the interface dipolar SBHM, and the solid lines fits to the extended SBHM with the bulk effect taken into account.

ranges found in *ab initio* calculations.[18] Considering these calculations were done for a planar Si/SiO_2 interface, one would expect better agreement for samples with a smaller vicinal angle, as is indeed the case. The O-Si-O angle distributions have significant weight around 107° according to Ref. 18, very close to $107.7° \pm 0.9°$ for $\zeta = 4°$ in our case. Table II shows that there is an overall decrease in the angle $\gamma_s + \gamma_t$ with increasing off-cut. This can be interpreted as a unique feature of the step edges which make an increasingly important contribution at large vicinal angles.

Figures 9(a) and 9(b) show the real and imaginary parts, respectively, of the bulk quadrupolar hyperpolarizability $\delta_b^{\parallel}$. The latter peaks at the photon energy 3.4 eV of the bulk E_1 resonance, instead of the redshifted energy 3.3 eV typical of interfacial contributions.[11] As with the preliminary results in Fig. 6, the real parts $\mathrm{Re}[\beta_s]$ of the step-edge hyperpolarizabilities [see Fig. 9(c)] depend strongly on vicinal angle, while $\mathrm{Re}[\beta_b]$ is again the least sensitive to vicinal angle, except for $\zeta = 10°$ and 0°.

As before, a nonlinear KK relation based on a single E_1-like resonance in $\mathrm{Im}[\beta_b]$ was explicitly enforced between $\mathrm{Im}[\beta_b]$ [panel (h)] and $\mathrm{Re}[\beta_b]$ [panel (g)]. In contrast to the results of Fig. 6, $\mathrm{Im}[\beta_{s,t}]$ [panels (d) and (f)] and $\mathrm{Im}[\delta_b]$ [panel (b)] now satisfy a qualitatively correct nonlinear KK relation with their corresponding real spectra. Specifically, $\mathrm{Im}[\beta_{s,t}]$ both exhibit positive peaks at $\hbar\omega_{\mathrm{SH}} \approx 3.3$ eV that are close to the zero crossing of the corresponding asymmetrically shaped $\mathrm{Re}[\beta_{s,t}]$. The relative amplitudes of real and imaginary $\beta(2\omega)$ are also approximately consistent with the KK relation for all bonds. This consistency reveals that the consideration of the bulk contribution in the SBHM is crucial in the correct representation of the microscopic nonlinear optical response.

The fitted $\mathrm{Im}[\delta_b]$ and $\mathrm{Im}[\beta_b]$ [Figs. 9(b) and 9(h)] both exhibit an E_1 peak at $\hbar\omega_{\mathrm{SH}} = 3.4$ eV, the E_1 critical point

TABLE II. Two upper bond angles γ_s and γ_t of the Si/SiO_2 interface tetrahedron defined with respect to [001] crystallographic direction. Uncertainties indicate the range of angles yielding a good fit to SHG data. Both interface dipolar and bulk quadrupolar contributions are taken into account in the calculation.

ζ	4°	6°	8°	10°
γ_s	$47.6° \pm 0.4°$	$49.23° \pm 0.2°$	$50.0° \pm 1.3°$	$45.9° \pm 1.4°$
γ_t	$60.1° \pm 0.5°$	$52.3° \pm 1.5°$	$38.8° \pm 3.5°$	$44.5° \pm 10.2°$

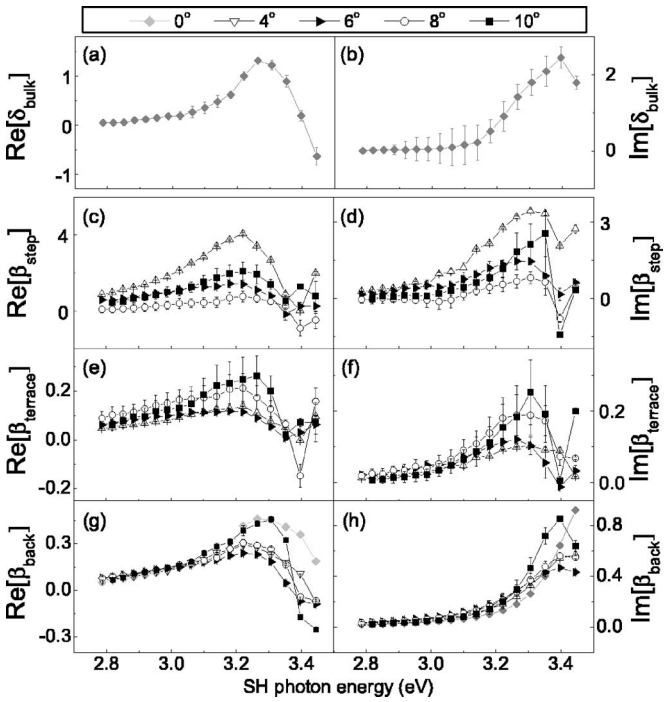

FIG. 9. Spectra of the fitted axial bulk quadrupolar hyperpolarizabilities δ_{bulk} [(a) and (b)] derived from the oriented Si/SiO_2:0° and the interface dipolar hyperpolarizabilities $\beta_j^{\parallel}$ of vicinal Si/SiO_2 offcut at $\zeta = 4°$, 6°, 8°, and 10° toward the [110] crystallographic direction [(c)–(h)]. The imaginary part of the back bond hyperpolarizability $\mathrm{Im}[\beta_{\mathrm{back}}]$ (h) was produced out of the $\mathrm{Re}[\beta_{\mathrm{back}}]$ through Kramers-Kronig relations. Error bars are correlated with uncertainty ranges in Table II.

resonance of bulk Si. The fitted $\mathrm{Im}[\beta_{s,t}]$ [(d), (f)] on the other hand, exhibit a redshifted E_1 peak at $\hbar\omega_{\mathrm{SH}} \simeq 3.3$ eV. The redshifted E_1 peak of the SHG spectra of Si/SiO_2, first observed by Daum *et al.*,[11] has been widely cited as a feature that distinguishes the interfacial Si/SiO_2 spectrum from that of bulk Si. The results of Fig. 9 suggest that this distinguishing feature is unique to the upper bonds of the interface tetrahedron.

Figure 10 shows, using the $\zeta = 6°$ hyperpolarizability spectra as an example, how improved KK consistency can be achieved by including E_1-like and E_2-like Lorentzian resonances in $\mathrm{Im}[\beta_j]$. The left-hand column [panels (a)–(c)] shows the results of the single (E_1-like) resonance KK analysis. The solid (dotted) curves show the real (imaginary) parts of the empirically fitted β_j, taken from Fig. 9. The filled (open) circles show corresponding real (imaginary) parts of β_j that exactly obey a KK relation within the framework of the single-resonance model. For the backbond (top), the empirically fitted and exact curves agree almost perfectly because the KK relation was explicitly enforced. For the step (middle) and terrace (bottom) bonds, they agree very well below the E_1 resonance, but diverge significantly above the resonance ($\hbar\omega > 3.3$ eV). This pattern is expected from the neglect of higher energy resonances in modeling $\mathrm{Im}[\beta]$, because the E_1 and higher energy resonances of $\mathrm{Im}[\beta]$ make contributions of opposite sign to $\mathrm{Re}[\beta]$ at frequencies just above the E_1 resonance. The right-hand column [panels (d)–

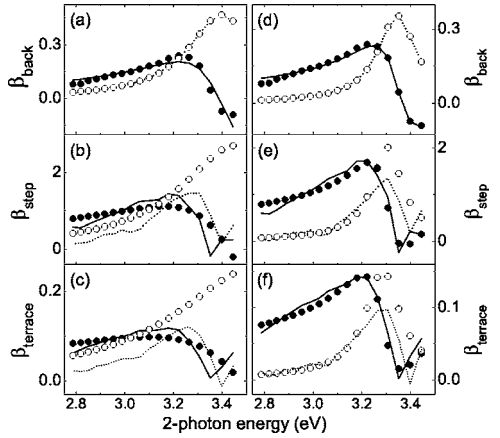

FIG. 10. Real (Solid curves) and imaginary (dotted curves) parts of empirically fitted hyperpolarizability spectra $\beta_j(\omega)$ for the $\zeta=6°$ sample, with relative phases of β_j adjusted to satisfy a nonlinear Kramers-Kronig relation based on either a single E_1-like resonance [panels (a)–(c)] or both E_1-like and E_2-like resonances [panels (d)–(f)] in Im[β_j]. Filled (open) circles show corresponding best-fit real (imaginary) parts of β_j that obey exact KK relations.

(f)] shows that the empirically fitted β_j agree much more closely with an exact KK relation when an optimized E_2-like resonance is included in Im[β]. The solid (dotted) curves are derived from the same empirical fit, and thus show the same relative phase among the β_j, as their counterparts in the left-hand column. However, spectral shapes differ for individual bonds—most notably for $\hbar\omega > 3.3$ eV—because of the different spectral phase imparted to β_j by the two-resonance model. In particular, Im[$\beta_{s,t}$] now show clearly defined Lorentzian E_1 resonances at 3.3 eV in good agreement with the exact two-resonance KK model. Similar improvements were found for the remaining samples. On the other hand, the KK *inconsistency* shown in Fig. 6 was not significantly remedied by invoking more sophisticated resonance models.

E. Final RAS reconstruction

The RAS was again reconstructed from linear polarizability $\alpha^{\parallel}$ derived from the interfacial hyperpolarizability [Figs. 9(c)–9(g)]. The result is shown in Fig. 11.

Figure 11 shows excellent reproduction of the RAS. Both the derivativelike shape and the monotonic increase of amplitude with vicinal angle were successfully reproduced. Representative experimental RAS data for $\zeta=6°$ (triangle) and 10° (square) in Fig. 11 confirm how closely the linear polarizability $\alpha^{\parallel}$ derived from the nonlinear $\beta^{\parallel}$ can generate the experimental RAS features.

F. Reconstruction of *s-p* SHG data

The set of $\beta_j^{\parallel}$, $\beta_{s,t}^{\perp}$, and/or $\delta^{\parallel}$ derived from fitting SHG data for the *p*-in/*p*-out polarization configuration provides all the necessary information required to predict SHG in other polarization configurations. We used the best fit parameters from the *p-p* data analysis to reconstruct the *s-p* SHG anisotropy [see Fig. 2(b)], using only an overall scaling factor to optimize the fit to the new data.

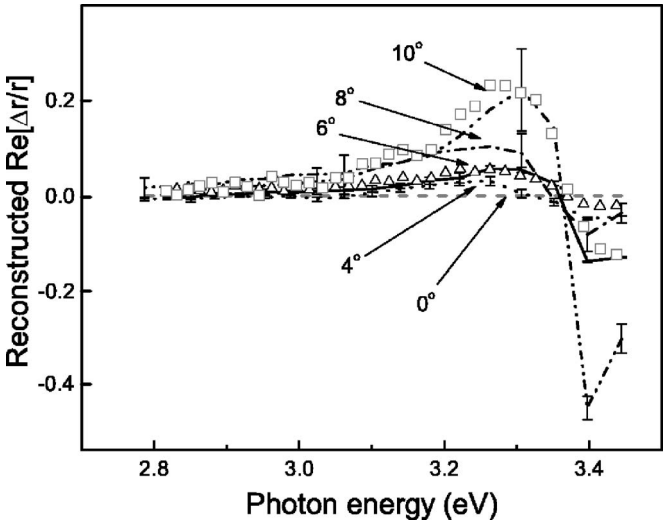

FIG. 11. Reconstructed RAS using the axial linear polarizabilities $\alpha_j^{\parallel}$ derived from fitted $\beta_j^{\parallel}$ in Fig. 9 with several representative error bars. Empty triangle and square represent the experimental data of $\zeta=6°$ and 10°, respectively. A single multiplication factor was applied to all the RAS reproduction to match the amplitude of the experimental data.

The reconstruction was carried out on all samples at each wavelength. Figure 12 shows a representative sampling of the results for the $\zeta=10°$ sample. It shows the corresponding *s-p* SHG data (dots) and reconstructed curves (solid). Generally, the reproduction is good. At all wavelengths ($h\nu_{SH} < 3.4$ eV) below the E_1 resonance it shows excellent agreement. Slight discrepancies become evident exactly on resonance (3.4 eV), but the χ^2 values are comparable to those achieved from fits to resonant *p-p* data with variable upper bond angles and bulk quadrupole contributions. Similar results were obtained for other samples. Thus, the fitted parameters are consistent with both *p-p* and *s-p* SHG data.

V. DISCUSSION

An advantage of SBHM over macroscopic phenomenological analysis is that the contribution of individual bonds

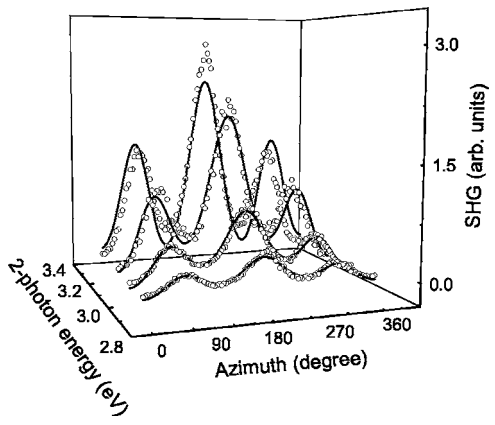

FIG. 12. The *s-p* SHG data (dotted) and the predicted anisotropy (solid) using parameters determined for *p-p*.

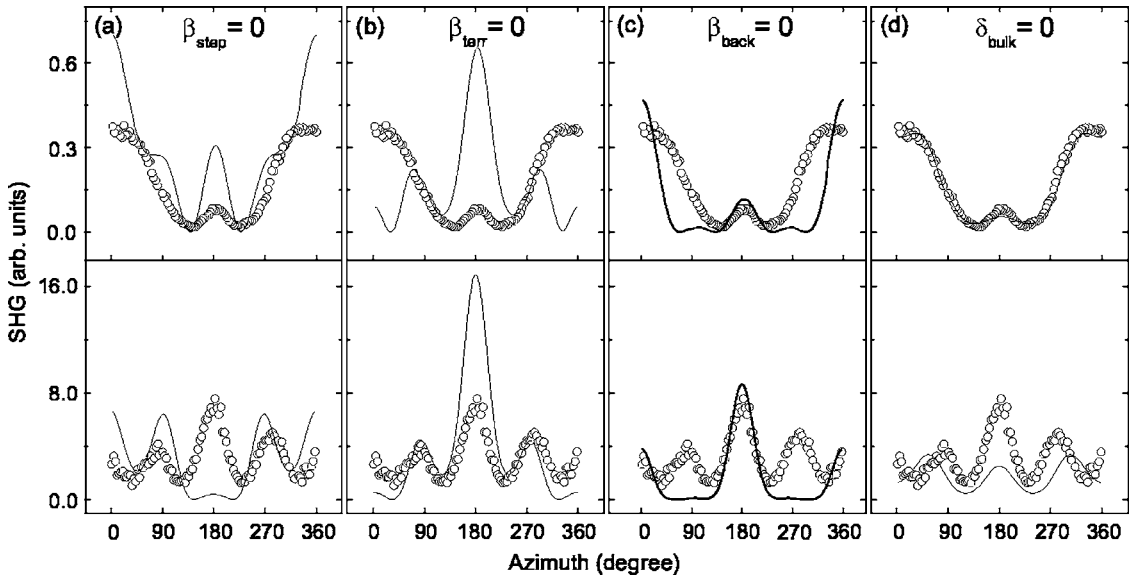

FIG. 13. Calculated SHG rotational anisotropy (solid curves) for $\zeta=4°$ at the SH photon energy of 2.8 eV (first row) and 3.3 eV (second row) when the contribution of step (a), terrace (b), back bond (c), and bulk (d) was removed. Experimental data (circles) are shown for comparison.

to SHG and RAS responses can be quickly evaluated by "turning off" selected $\beta_j^{\parallel}$ or $\alpha_j^{\parallel}$. As an example, Fig. 13 shows the effect on the SHG response of zeroing each bond contribution one by one at two SH photon energies, one far away from resonance (2.8 eV, first row), the other at resonance (3.3 eV, second row) for the $\zeta=4°$ sample. Column (a) shows the result of setting $\beta_{\text{step}}=0$. Below resonance, the center peak at 180° intensifies, while at resonance it weakens. Eliminating the terrace contribution, on the other hand, strengthens the 180° maximum in both resonance and nonresonance cases as shown in column (b). Setting $\beta_{\text{back}}=0$ primarily affects the azimuth 90° (or 270°) peak, decreasing the amplitude [column (c)]. Removing δ_{bulk} yields negligible change far from resonance, but a significant change at (or near) resonance [Fig. 13(d)].

In order to see these effects in terms of symmetry change, we used a Fourier sum Eq. (1) to analyze Fig. 13. Figure 14 compares the Fourier coefficients for $\beta_{\text{step}}=0$, $\beta_{\text{terrace}}=0$, $\beta_{\text{back}}=0$, and $\delta_{\text{bulk}}=0$ to their values when all bonds contribute. Below resonance [Fig. 14(a)], setting $\beta_{\text{step}}=0$ strengthened a_0 as well as a_2 and a_4. Meanwhile, it has a very different effect at 3.3 eV. The phase of a_1, a_2, and a_3 were reversed, and the absolute amplitude of a_1 and a_2 increased. a_0 and a_4 change very little. Overall, the step bond influences all Fourier components. The terrace bond, on the other hand, has its greatest impact on a_1, reversing the phase at 2.8 eV and increasing the amplitude at 3.3 eV. There is a significant amount of isotropic contribution from the backbonds (see the fourth column of a_0). They also balance the twofold symmetry; terminating β_{back} intensified a_2 amplitude greatly. The bulk is the sole source of a_4 because the last column of a_4's in Fig. 14 disappeared when $\delta_{\text{bulk}}=0$.

We carried out a similar bond-by-bond analysis of RAS. Figure 15 shows the reproduced RAS response for $\zeta=4°$ when only step α_{step}, terrace α_{terr}, or backbond α_{back} polarizability is present. Since $\Delta r/r=2(r_{1\bar{1}0}-r_{110})/(r_{1\bar{1}0}+r_{110})$, step and terrace bonds, which are parallel to [110] produce RAS with opposite sign to that of the backbonds, which are parallel to $[1\bar{1}0]$ (see Fig. 5).

Unlike the SHG, they all produce similar spectroscopic shape. The derivativelike RAS pattern comes from the larger amplitude of $\Delta r/r$ of [110] components (i.e., step and terrace) after 3.3 eV which is smaller than or equal to that of $[1\bar{1}0]$ (i.e., backbonds) before 3.3 eV.

This exercise of examining the response of SHG and RAS to the individual polarizable unit suggested that each bond of the interface and bulk tetrahedron contributes in an equally significant way to both spectra.

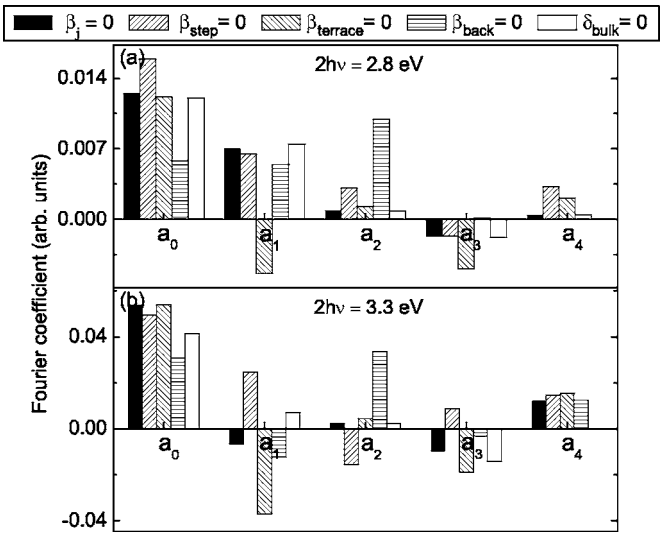

FIG. 14. Fourier coefficients corresponding to Fig. 13 at SH photon energy 2.8 (a) and 3.3 eV (b).

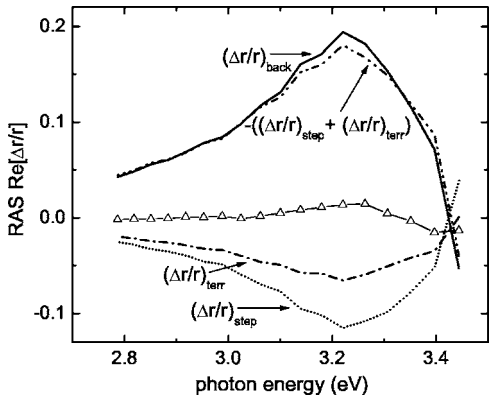

FIG. 15. Reproduced RAS for $\zeta=4°$ (empty triangle), same as that of Fig. 11 shown together with RAS patterns when only step (dotted line), terrace (dash-dot), and backbond (solid line) contribution exists, respectively. The RAS reproduced with step and terrace bond contribution together is shown with its sign flipped (dash-dot-dot) for comparison.

VI. CONCLUSION

We have presented experimental spectroscopic SHG and RAS data for oxidized vicinal Si(001) samples with five different off-cut angles. The SHG rotational anisotropy spectra were analyzed using an extended version of the SBHM. RAS were then reconstructed using results derived from the SBHM analysis of SHG spectra. The nonlinear and linear spectroscopies were thereby linked to a common microscopic model. Successful reproduction of RAS measurements and Kramers-Kronig consistency between the fitted real and imaginary hyperpolarizability spectra of each bond relied critically on incorporation of the bulk quadrupole contribution to SHG. The extended SBHM with this addition was implemented without increasing the number of free parameters by fitting the fourfold anisotropic SHG of oriented $Si(001)/SiO_2$. The main RAS features—derivative line shape close to the E_1 critical point and the monotonic increase of the RAS amplitude with the vicinal angle—were all reproduced in this case. Results suggest existence of a common microscopic model of RAS and SHG, which thus motivates studies of clean surfaces with well-characterized structure. We also examined the individual bond contribution to RAS and SHG rotational anisotropy spectroscopy.

ACKNOWLEDGMENTS

This research was supported by the Robert Welch Foundation (Grant No. F-1038) and NSF Grants No. DMR-0207295 and No. PHY-0114336.

[1] G. Lüpke, Surf. Sci. Rep. **35**, 75 (1999).
[2] D. E. Aspnes and A. A. Studna, Phys. Rev. Lett. **54**, 1956 (1985).
[3] M. C. Downer, B. S. Mendoza, and V. I. Gavrilenko, Surf. Interface Anal. **31**, 966 (2001).
[4] V. I. Gavrilenko, R. Q. Wu, M. C. Downer, J. G. Ekerdt, D. Lim, and P. Parkinson, Phys. Rev. B **63**, 165325 (2001).
[5] *Epioptics: Linear and Nonlinear Optical Spectroscopy of Surfaces and Interfaces* edited by J. McGilp, D. Weaire, and C. Patterson (Springer-Verlag, Berlin, 1995).
[6] Jinhee Kwon and M. C. Downer, Phys. Status Solidi C **0**, 3055 (2003).
[7] G. Lüpke, D. J. Bottomley, and H. M. van Driel, J. Opt. Soc. Am. B **11**, 33 (1994).
[8] G. D. Powell, J. F. Wang, and D. E. Aspnes, Phys. Rev. B **65**, 205320 (2002).
[9] J. -K. Hansen, H. J. Peng, and D. E. Aspnes, J. Vac. Sci. Technol. B **21**, 1798 (2003).
[10] N. Arzate and B. S. Mendoza, Phys. Rev. B **63**, 113303 (2001).
[11] W. Daum, H.-J. Krause, U. Reichel, and H. Ibach, Phys. Rev. Lett. **71**, 1234 (1993).
[12] C. Flytzanis and J. Ducuing, Phys. Rev. **178**, 1218 (1969).
[13] R. C. Miller, Appl. Phys. Lett. **5**, 17 (1964).
[14] J. G. Mihaychuk, N. Shamir, and H. M. van Driel, Phys. Rev. B **59**, 2164 (1999).
[15] D. E. Aspnes, J. P. Harbison, A. A. Studna, and L. T. Florez, J. Vac. Sci. Technol. A **6**, 1327 (1988).
[16] S. Scandolo and F. Bassani, Phys. Rev. B **51**, 6925 (1995).
[17] K.-E. Peiponen, V. Lucarini, J. J. Saarinen, and E. Vartiainen, Appl. Spectrosc. **58**, 499 (2004).
[18] A. A. Demkov and O. F. Sankey, Phys. Rev. Lett. **83**, 2038 (1999).
[19] E. Schroder-Bergen and W. Ranke, Surf. Sci. **259**, 323 (1991).
[20] J. F. McGilp and L. Carroll, Phys. Status Solidi C **0**, 3060 (2003).
[21] N. Bloembergen and D. S. Pershan, Phys. Rev. **128**, 606 (1962).